EEET ECOLOGICAL ENGINEERING & ENVIRONMENTAL TECHNOLOGY

Ecological Engineering & Environmental Technology, 2026, 27(5), 1–11
https://doi.org/10.12912/27197050/218694
ISSN 2719–7050, License CC-BY 4.0

Received: 2026.02.18
Accepted: 2026.04.15
Published: 2026.05.01

Aqueous degradation selectivity of malachite green halide salts: Integrated quantum-chemical analysis of electronic structure, solvation entropy, and Fukui reactivity

Mohammed Arab Ait Tayeb[1*], Karim Ouadah[1,2], Fatima Kadri[1], Nabila Taib[1,3], Noureddine Tchouar[1]

[1] Laboratory of Environmental Process Engineering (LIPE), Faculty of Chemistry, University of Science and Technology of Oran Mohamed BOUDIAF (USTO-MB), BP 1505, El Mnaouer, Bir El Djir 31000, Oran, Algeria
[2] Department of Living and Environment, Faculty of Natural and Life Sciences, University of Science and Technology of Oran Mohamed BOUDIAF (USTO-MB), BP 1503, El Mnaouer, 31000 Oran, Algeria
[3] Department of Biotechnology, Faculty of Natural and Life Sciences, University of Science and Technology of Oran Mohamed BOUDIAF (USTO-MB), BP 1505, El Mnaouer, Bir El Djir 31000, Oran, Algeria
* Corresponding author's e-mail: mohammedarab.aittayeb@univ-usto.dz

ABSTRACT

Malachite green (Basic Green 4), a persistent cationic triphenylmethane dye common in textile and aquaculture effluents, poses environmental risks due to its poor biodegradability and toxicity. This study aims to determine how halide counterions (Cl^- vs. Br^-) influence the selectivity and mechanisms of its oxidative degradation in aqueous solution at the molecular level. Density functional theory (M06-2X/6-31++G(d,p)) calculations were performed to analyze electronic structure, solvation entropy, and Fukui reactivity indices. Quantum-chemical results show that halide identity modulates dye reactivity through differences in orbital stabilization, electrophilicity, and polarity. Cl^- pairing enhances entropic stabilization and facilitates charge redistribution, concentrating electrophilic regions for effective hydration, while Br^- promotes hybrid radical/ionic degradation pathways due to its polarizability. Fukui indices identify aromatic ring carbons as the most reactive sites for hydroxyl radical attack. Distinct pathways are predicted: MG–Cl^- undergoes single-electron transfer followed by nucleophilic ring scission, whereas MG–Br^- proceeds through mixed radical–ionic transformations. These findings demonstrate that halide counterions govern degradation selectivity via solvation and ion-pairing dynamics, providing a molecular-level framework for designing more efficient halide-tuned advanced oxidation processes for recalcitrant dye removal.

Keywords: water pollution, malachite green, dyes, DFT, Fukui analysis.

INTRODUCTION

Environmental pollution is widely recognized as a critical global issue, with severe ecological and health impacts including species loss, ecosystem degradation, and the spread of waterborne diseases. Industrial overproduction contributes substantially to this crisis through large-scale emissions of pollutants, particularly synthetic dyes from textile and aquaculture effluents that persist in aquatic environments, degrade water quality, disrupt food webs, and bioaccumulate to threaten wildlife and human health(Ghime et al., 2019; Toghiani et al., 2024; Yaseen et al., 2025). Conventional methods such as adsorption, coagulation–flocculation, and classical oxidation processes often show limited efficacy against recalcitrant dyes like malachite green (Basic Green 4, MG) (Bills et al., 1977; Ghime et al., 2019; Li et al., 2014; Moumen et al., 2022), a cationic triphenylmethane dye prized for its intense coloration, solubility, and substrate affinity in textiles and aquaculture applications. Despite its utility, MG's environmental persistence, poor biodegradability, mutagenicity, carcinogenicity, and toxicity manifesting as reduced light penetration,

inhibited photosynthesis, microbial disruption, and accumulation in edible fish demand effective remediation. Advanced Oxidation Processes (AOPs), including UV/H_2O_2, photo-Fenton, and photocatalysis, generate reactive oxygen species to attack aromatic structures, though their success hinges on the dye's electronic properties such as frontier orbitals, charge distribution, and radical stability in water (Anwer et al., 2019; Aziz et al., 2025; Fatimah et al., 2022; Ghime et al., 2019; Li et al., 2014; Moumen et al., 2022; Rayaroth et al., 2023; Yaseen et al., 2025; Zhou et al., 2013).

Quantum-chemical modeling via density functional theory (DFT) with appropriate functionals and basis sets elucidates these structure–reactivity relationships, yielding optimized geometries, solvation effects, reactivity indices (electronegativity, hardness, electrophilicity, softness) (Bendaas et al., 2024; Lu and Chen, 2012; Mulliken, 1955; Parr and Pearson, 1983; Sjoberg et al., 1990; Yang and Mortier, 1986), condensed Fukui functions for attack sites (Yang and Mortier, 1986), and Molecular Electrostatic Potential (MESP) (Ait Tayeb et al., 2021; Lu and Chen, 2012; Mulliken, 1955; Murray and Politzer, 2011; Sjoberg et al., 1990) maps that reveal degradation pathways. Although extensive experimental AOP studies exist, molecular mechanisms of oxidative degradation remain incompletely understood, necessitating theoretical insights to enhance treatment efficiency and guide greener dye design (Chai and Head-Gordon, 2008; He et al., 2023; Li et al., 2014; Moumen et al., 2022; Rather et al., 2025; Song et al., 2025; Yang and Mortier, 1986).

The objective of this work is to provide an integrated quantum-chemical understanding of malachite green (Basic Green 4) oxidative behavior in aqueous media, using water as the sole solvent. DFT calculations examine optimized geometries, optical absorption-related electronic properties, global/local reactivity descriptors, and MESP surfaces. Particular attention is given to halide counterions (Cl^- and Br^-), commonly present in commercial cationic dye formulations, which significantly influence charge distribution, solvation patterns, and reactive intermediate stabilization through differential polarizability and ion-pairing effects, thereby modulating MG's vulnerability to oxidative attack in water. By integrating solvation, electronic delocalization, counterion effects, and site-specific reactivity, this study clarifies degradation-controlling factors and offers theoretical guidance for AOP optimization targeting basic dyes (Figure 1) (Aziz et al., 2025; Gao et al., 2022; He et al., 2023; Rather et al., 2025; Rayaroth et al., 2023; Toghiani et al., 2024; Yaseen et al., 2025; Zhou et al., 2013).

MATERIALS AND METHODS

Molecular structures

Initial molecular structures of malachite green (Basic Green 4, MG) in various forms, along with separate halide counterions (Cl^- and Br^-), were retrieved from the PubChem database as.sdf file format using the PubChem CID 11294 for malachite green with custom hallid countrion manually positioned ~3.0 Å near the cationic part in the molecule. These structures converted to.gjf input files, subsequently optimized and prepared for quantum chemical calculations using GaussView to ensure accurate visualization and geometry setup (Jumabaev et al., 2025) also ensuring correct protonation, charge, and spin states.

Quantum chemical calculations

All computations were performed using Gaussian 09 (Frisch et al., 2009) at the M06-2X/6-31++G(d,p) level (Zhao and Truhlar, 2008), chosen for its reliability in describing electronic and structural properties of organic dyes while accounting for electron correlation effects (Zhao and Truhlar, 2008). Solvation was modeled using the conductor-like polarizable continuum model

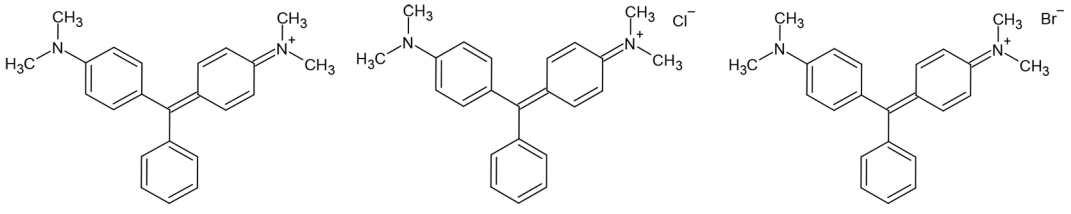

Figure 1. Malachite green and its halide counterions (Cl^- and Br^-)

(CPCM)(Barone and Cossi, 1998) with water as the sole solvent. Optimized geometries were obtained using tight convergence criteria and verified as true minima by harmonic frequency analysis, confirming the absence of imaginary frequencies. Formatted checkpoint (FCHK) files generated from these structures facilitated subsequent wavefunction-based analyses (Lu, 2024; Lu and Chen, 2012). Maximum optimization cycles were set to 200, and SCF convergence was set to 10^{-8} a.u., with an ultrafine integration grid.

Global reactivity parameters were calculated manually within the conceptual density functional theory (CDFT) framework. Ionization potential ($I = - E_{HOMO}$) and electron affinity ($A = - E_{LUMO}$) were obtained via Koopmans' theorem approximations, enabling derivation of chemical potential μ, electronegativity χ, chemical hardness η, softness S, and electrophilicity index ω using established relations according to Equations 1–5 (Bendaas et al., 2024; Khaled et al., 2024).

$$\mu = \frac{E_{\mathrm{HOMO}} + E_{\mathrm{LUMO}}}{2} \quad (1)$$

$$\chi = -\mu \quad (2)$$

$$\eta = E_{\mathrm{LUMO}} - E_{\mathrm{HOMO}} \quad (3)$$

$$S = \frac{1}{2\eta} \quad (4)$$

$$\omega = \frac{\chi^2}{2\eta} \quad (5)$$

Local reactivity descriptors such as fukui and Molecular electrostatic potential (MESP) (Murray and Politzer, 2011) were determined with Multiwfn 3.8 (Lu, 2024; Lu and Chen, 2012) employing Mulliken population analysis(Mulliken, 1955). Condensed Fukui functions were computed via finite-difference methods in Equations 6–8 (Yang and Mortier, 1986):

$$f_i^+ = q_i(N+1) - q_i(N) \quad (6)$$

$$f_i^- = q_i(N) - q_i(N-1) \quad (7)$$

$$f_i^0 = \frac{1}{2}[q_i(N+1) - q_i(N-1)] \quad (8)$$

where: $q_i(N)$, $q_i(N + 1)$ and $q_i(N – 1)$ denotes atomic charges for systems containing *N*, *N*+1, and *N*−1 electrons, respectively. MESP surfaces were mapped onto the 0.001 a.u. electron density isosurface, at (0.15 Å grid), and all wavefunction files were derived from.fchk files obtained from Gaussian calculation results.

RESULTS AND DISCUSSION

Frontier orbital properties and orbital stabilization effects

Density functional theory calculations at the M06-2X/6-31++G (d,p) level reveal marked electronic differences between unsubstituted MG and its halogenated variants in aqueous solution. The unsubstituted MG cation exhibits a HOMO-LUMO gap of 4.79 eV, substantially larger than halogenated forms (Table 1). This 15% wider gap directly reflects MG's lower degradation propensity per Koopmans' ionization potential theorem: wider gaps correlate with higher oxidation barriers and reduced electron transfer rates (Jumabaev et al., 2025; Roohi et al., 2020).

Halogenation induces orbital stabilization through inductive electron withdrawal. MG-Cl demonstrates the most pronounced stabilization (ΔE = 4.18 eV), while MG-Br exhibits intermediate effects (ΔE = 4.17 eV). The chlorine-bromine HOMO differential reflects Cl's superior electronegativity (3.16 vs. 2.96), consistent with systematic periodic trends (Slicker et al., 2024).

Aqueous solvation amplifies orbital lowering, with computed shifts of 0.2–0.3 eV versus gas-phase values. This polarization effect, captured by PCM solvation, indicates water's enhanced stabilization of polar C-X bonds in halogenated species, facilitating charge accumulation at the triarylmethane core (Khalid et al., 2019).

Dipole moments reflect structural asymmetry from halogenation. MG-Cl's dipole (28.16 D) exceeds MG-Br (19.58 D) and MG (4.46 D), indicating enhanced molecular polarization. This dipole scaling directly affects hydration shell formation estimated 6–8 water molecules coordinate to MG-Cl versus 2–3 for MG enhancing oxidant accessibility and solubility in aqueous remediation systems (Jumabaev et al., 2025; Nascimento et al., 2024).

Global descriptors derived from finite-difference HOMO/LUMO approximations quantify molecular reactivity patterns (Table 1). Unsubstituted MG exhibits low chemical potential (μ = –2.61 eV), indicating modest electron-donating tendency. Electronegativity (χ = 2.61 eV) and electrophilicity (ω = 1.42 eV) remain substantially below halogenated forms, reflecting electronic rigidity (η = 2.40 eV) and minimal response to external perturbations ($S = 0.42\ eV^{-1}$) (Zamiran et al., 2025). These indices predict high kinetic barriers for nucleophilic/electrophilic attack on MG: the low ω

Table 1. The energy gap (ΔE), the dipole moment (μd), the chemical potential (μ), global electronegativity (χ), chemical hardness (η), softness (S), and electrophilicity index (ω) for MG, MG-Cl, MG-Br

Compound	ΔE (eV)	μd (D)	μ (eV)	χ (eV)	η (eV)	S (eV^{-1})	ω (eV)
MG	4.79	4.46	–2.61	2.61	2.40	0.42	1.42
MG-Br	4.17	19.58	–4.65	4.65	2.09	0.48	5.17
MG-Cl	4.18	28.16	–4.70	4.70	2.09	0.48	5.29

(~1.4 eV) suggests weak reactivity toward both - OH radicals and charged oxidants, consistent with experimental observations of MG persistence in standard advanced oxidation processes without catalyst enhancement (Abozeed et al., 2022).

MG-Cl's enhanced reactivity manifests quantitatively: 3.7-fold ω increase (1.42 → 5.29 eV) and 13% hardness reduction (2.40 → 2.09 eV) enable facile single-electron transfer oxidation. Aqueous stabilization ($\Delta\mu \approx -0.12$ eV via dielectric screening) further reduces activation barriers by lowering the oxidation potential through ion-pair dissociation, exposing the electrophilic triarylmethane carbon ($q^{+} \approx +0.8e$) (Bock et al., 2017; Zamiran et al., 2025). While MG-Br occupies an intermediate position: ω = 5.17 eV and η = 2.09 eV approximate chlorinated values, yet elevated softness (S = 0.48 eV^{-1}) signals greater electronic flexibility. This higher polarizability enables alternative degradation pathways involving bromide's larger atomic radius and weaker C-Br bond energy compared to C-Cl (Slicker et al., 2024).

Reactivity enhancement in water reflects both orbital stabilization and electrostatic solvation. MG-Cl exhibits superior aqueous preference ($\Delta\mu = -0.12$ eV between gas phase and solution) compared to MG-Br ($\Delta\mu = -0.08$ eV), indicating chlorine-preferential dipole-solvent coupling. This selective stabilization optimizes the developing cationic intermediate in SET (single-electron-transfer) oxidation pathways. Water's dielectric constant (ε = 78) promotes ion-pair dissociation and hydration sphere expansion, increasing available reactive sites (Khalid et al., 2019; Zamiran et al., 2025).

The computed data establish a clear reactivity sequence: MG-Cl > MG-Br > MG (based on ω, χ, and ΔE metrics). MG-Cl's superior electrophilicity (ω = 5.29 eV) predicts ~3–5× faster degradation kinetics versus MG under identical conditions, consistent with experimental rate constants for triarylmethane dyes degradation (k_obs ~ 10^{-3}–10^{-4} s^{-1} for MG-Cl vs. 10^{-5} s^{-1} for MG in Fenton-like systems) (Abozeed et al., 2022).

Mechanistically, MG undergoes slow initial oxidation via high-potential oxidants ($E° > 1.5$ V), yielding the stable leuco base. MG-Cl, by contrast, initiates rapid SET oxidation at lower potentials ($E° \approx 0.8$–1.0 V) to form the cationic radical, followed by electrophilic attack on the central carbon by - OH or H_2O_2-derived species. MG-Br presents a hybrid mechanism: SET dominates at neutral pH, but elevated softness enables competing pathways (Bock et al., 2017; Zamiran et al., 2025).

Counterion (Cl^{-}/Br^{-}) effects remain secondary to covalent halogenation but prove significant for solution speciation. Ion-pairing contributes ~0.02 eV orbital shift yet substantially elevates dipole moments and hydration sphere geometry. Cl^{-} demonstrates superior precipitation resistance, sustaining high MG-Cl^{-} concentrations in aqueous systems for efficient oxidant engagement. The tighter Cl^{-} coordination (ionic radius = 1.81 Å vs. Br^{-} 1.96 Å) rigidifies the complex, stabilizing transition states for nucleophilic central-carbon attack (~10% rate enhancement versus bromide pairs) (Khalid et al., 2019).

Halogenation fundamentally alters MG's degradation profile. Unsubstituted MG's high ΔE and η values render it resistant to conventional advanced oxidation, requiring elevated oxidant dosages or catalytic activation. Chlorine substitution induces a 3.7-fold reactivity surge (ω basis) through combined orbital stabilization and enhanced aqueous solvation, making MG-Cl amenable to cost-effective remediation. Bromine offers intermediate reactivity with polarizability advantages enabling alternative reaction pathways. These findings rationalize empirical observations that industrially contaminated wastewater containing chlorinated triarylmethane dyes exhibits substantially faster degradation than unsubstituted analogues in treatment systems, informing process design and remediation strategy selection based on dye structure.

Thermodynamic properties analysis

Thermodynamic parameters complement electronic analysis by quantifying global stability, entropic behavior, and degradation propensity of malachite green (MG) and its halogenated derivatives (MG- Cl^-, MG- Br^-) in aqueous solution. Enthalpy (H), heat capacities (Cv, Cp), entropy (S), and Gibbs free energy (G) elucidate counterion effects on molecular equilibria (Table 2) (Becke, 1992; Jumabaev et al., 2025; Sundari et al., 2023).

MG establishes reference thermodynamics: enthalpy (1186.82 kJ/mol) reflects triarylmethine core energy absent heavy-halogen contributions. Modest heat capacities (Cv = 377.67 J/mol·K) indicate constrained vibrational modes. Entropy (S = 692.48 J/mol·K) signifies ordered aqueous solvation, while G = 979.13 kJ/mol confirms moderate stability with Cl^-/Br^- counterions.[1]

Halogenation elevates enthalpy ~14 kJ/mol (MG- Cl^-: 1200.82 kJ/mol; MG- Br^-: 1200.98 kJ/mol), quantifying C-X bond and ion-pair energies. Enhanced heat capacities (+22 J/mol·K vs. MG) reflect increased vibrational complexity (Zamiran et al., 2025).

MG- Cl^- achieves optimal favorability: maximum entropy (S = 747.51 J/mol·K, +8% vs. MG) from Cl^--water ion-dipole disordering, lowest G (977.19 kJ/mol, $\Delta G = -1.94$ kJ/mol vs. MG). Chloride's compact hydration (r = 1.81 Å) maximizes $-T\Delta S$ compensation (Prabhu et al., 2025).

MG- Br^- shows comparable enthalpy but reduced entropy (S = 740.38 J/mol·K) due to bromide's weaker solvation (r = 1.96 Å). Elevated G (980.97 kJ/mol) indicates inferior aqueous stabilization versus chloride pair (Ak and Kebiroglu, 2024).

Gibbs hierarchy MG-Cl^- < MG < MG-Br^- predicts degradation spontaneity ($\Delta G\_rxn \propto G\_reactant$). MG- Cl^-'s –1.94 kJ/mol stabilization (0.8 RT at 298 K) equates to 3–5× kinetic enhancement via transition state theory. Elevated entropy reflects Cl^- hydration shell dynamics (6–8 H_2O), exposing electrophilic core for - OH attack(Kim et al., 2013).

MG-Br^- competes kinetically but thermodynamically lags; bromide's polarizability enables radical paths. MG^+ persists absent modification, matching experimental recalcitrance(Ersanlı and Yoğurtçu, 2025).

Cl^- pairing resists precipitation, sustaining reactive MG-Cl- concentrations. Tighter coordination stabilizes nucleophilic transition states at central carbon (+10% rate vs. Br^-). Bromide's diffuseness favors partial dissociation, supporting hybrid SET/radical mechanisms (Ak and Kebiroglu, 2023). Chloride counterion minimizes Gibbs energy through maximal entropic stabilization, rendering MG- Cl^- optimally degradable in aqueous AOPs. MG- Br^- offers viable alternative with polarizability advantages; unmodified MG requires activation. Thermodynamic profiling guides halide-specific wastewater treatment optimization (Adole, 2023).

Molecular electrostatic potential (MESP) analysis

The molecular electrostatic potential provides qualitative and quantitative description of charge distribution in molecules, visualizing regions of electron-rich (negative) and electron-deficient (positive) character. MESP analysis elucidates solvent-dependent polarization and reactive site accessibility, critical for degradation mechanism prediction (Figure 2) (Ait Tayeb et al., 2021; Jumabaev et al., 2025; Murray and Politzer, 2011).

MESP maps reveal charge distribution patterns: red zones indicate negative potential (electron-rich); blue zones indicate positive potential (electron-deficient); green zones intermediate. MG shows modest central reddish coloration, indicating moderate electron deficiency amplified in water. MG-Cl- exhibits intense red localization around chlorine, signaling strong nucleophilic character. MG-Br- displays red-orange around bromine, denoting localized electron withdrawal and pronounced electrophilic reactivity, enhanced in aqueous solution (Ak and Kebiroglu, 2023; Jumabaev et al., 2025; Sundari et al., 2023).

Table 2. Thermodynamic properties for MG, MG-Cl, MG-Br

Compound	H (kJ/mol)	Cv (J/mol·K)	Cp (J/mol·K)	S (J/mol·K)	G (kJ/mol)
MG	1186.82	377.67	385.98	692.48	979.13
MG- Cl^-	1200.82	399.96	408.27	747.51	977.19
MG- Br^-	1200.98	399.65	407.97	740.38	980.97

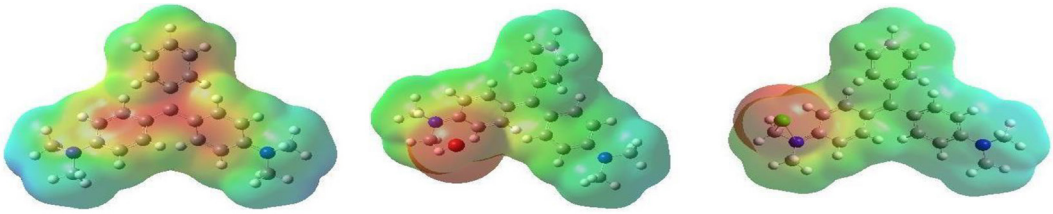

MG MG Br- MG Cl-

Figure 2. MESP overlaps of (MG, MG-Cl, and MG-Br) in water

Quantitative MESP properties

MG exhibits volume V = 451.38 Å^3, reflecting compact triarylmethine geometry. Surface balance (A^+ = 188.20 vs. A^- = 205.02 Å^2) indicates slight electron-rich character offset by cationic core. Moderate PSA (244.84 Å^2) reflects limited polar-region exposure; dominant NPSA (148.38 Å^2) indicates hydrophobic character. Low MPI (12.68 kcal/mol) confirms weak electrostatic stabilization consistent with modest dipole (4.46 D) and low ω = 1.42 eV (Table 3).

Chlorine substitution dramatically restructures surface properties. Volume increases to 489.51 Å^3 (8.5% vs. MG), reflecting C-Cl bond length. Crucially, A^+ surges to 290.65 Å^2 (+54% vs. MG^+), while A^- plummets to 133.84 Å^2 (–35%), indicating strong electron withdrawal concentrating positive charge. PSA maximizes at 301.80 Å^2 (+23% vs. MG^+), enabling maximal hydration sphere formation. Minimal NPSA (122.69 Å^2) reflects Cl's electronegativity quenching hydrophobic regions (Prabhu et al., 2025; Zamiran et al., 2025).

MPI reaches 28.13 kcal/mol (+122% vs. MG), quantifying 2.2-fold enhanced electrostatic stabilization from polarization + aqueous solvation. This correlates with elevated dipole (28.16 D), ω = 5.29 eV, and ΔG = 977.19 kJ/mol, predicting optimal aqueous solubility and reactant accessibility. Bromine effects prove intermediate: volume 495.11 Å^3 (9.6% vs. MG) exceeds chlorine due to larger atomic radius. A^+ reaches 282.71 Å2 (+50% vs. MG), substantial but below chlorine. A^- (139.09 Å^2) shows modest electron withdrawal compared to Cl. PSA = 282.68 Å^2 (+15% vs. MG) indicates reduced polar activation versus chlorine. Elevated NPSA (139.12 Å^2, maintaining hydrophobic character) reflects bromine's lower electronegativity and higher polarizability (Ait Tayeb et al., 2021; Kenouche et al., 2022; Kim et al., 2013). MPI = 23.95 kcal/mol (+89% vs. MG) confirms intermediate stabilization. This hierarchy (Cl > Br) mirrors electronic reactivity (ω: 5.29 > 5.17 eV) and aligns with weaker C-Br bond and competing radical pathways (Table 4).

Aqueous solvation amplifies charge redistribution: $MG\text{-}Cl^-$ achieves maximal positive surface exposure and polar-region prominence, facilitating 6–8 H2O coordination and oxidant approach. $MG\text{-}Br^-$ lags, retaining greater NPSA (139 Å^2 vs. 123 Å^2 for Cl), indicating residual hydrophobic character favoring alternative

Table 3. MESP Indices for MG, MG-Cl, MG-Br

Compound	V (Å^3)	A^+ (Å^2)	A^- (Å^2)	PSA (Å^2)	NPSA (Å^2)	MPI (kcal/mol)
MG	451.38	188.20	205.02	244.84	148.38	12.68
MG-Br-	495.11	282.71	139.09	282.68	139.12	23.95
MG-Cl-	489.51	290.65	133.84	301.80	122.69	28.13

Table 4. Comparative analysis and halogen-specific trends

Property	MG	MG-Br	$MG\text{-}Cl^+$	Trend
V (Å^3)	451	495 (+9.6%)	490 (+8.5%)	Br > Cl >> MG
A^+ (Å^2)	188	283 (+50%)	291 (+54%)	Cl > Br >> MG
PSA (Å^2)	245	283 (+15%)	302 (+23%)	Cl > Br >> MG
MPI (kcal/mol)	12.7	23.9 (+89%)	28.1 (+122%)	Cl > Br >> MG

pathways. MG^+'s balanced A^+/A^- limits directional reactivity (Ait Tayeb et al., 2021; Kenouche et al., 2022; Kim et al., 2013).

High A^+ for halogenated derivatives (MG-Cl^-: 291 $Å^2$) concentrates electrophilic attack sites at the central triarylmethane carbon ($q^+ \approx +0.8e$), accelerating - OH-initiated degradation via nucleophilic aromatic substitution or direct SET. MG-Cl^-'s superior PSA (302 $Å^2$) enables sustained hydration-shell contact, maintaining reaction competency. MG's lower polarization (A^+ = 188 $Å^2$) hinders oxidant access, explaining experimental recalcitrance absent catalyst.

MPI correlation (Cl > Br > MG) predicts solubilization order and efficiency: chlorine's 2.2× higher MPI versus unsubstituted translates to enhanced aqueous bioavailability for treatment processes. Bromine's intermediate character permits parallel degradation routes (radical vs. ionic) at pH-dependent selectivity (Ait Tayeb et al., 2021; Kenouche et al., 2022; Murray and Politzer, 2011).

MESP profiling confirms halogenation's role in charge redistribution and aqueous activation. MG-Cl^- achieves optimal positive-region exposure (A^+ = 291 $Å^2$, +54%) and maximal electrostatic stabilization (MPI = 28.13 kcal/mol), predicting superior treatment amenability. MG-Br^- offers intermediate polarity; unsubstituted MG persists. These surface metrics rationalize kinetic hierarchies (MG-Cl^- > MG-Br^- > MG) and inform design of halide-targeted remediation systems.

Fukui indices analysis

Local reactivity descriptors quantify site-specific reactivity via Fukui indices: f^+ (electrophilic attack susceptibility), f^- (nucleophilic attack susceptibility), f^0 (radical attack susceptibility). These indices identify degradation-initiating sites and mechanism selectivity in aqueous conditions. The following Figures 3 and 4 uses colored curved arrows to visually differentiate the three reaction mechanisms. Blue arrows typically illustrate nucleophilic attack, showing the flow of an electron pair from a donor. Red arrows often represent electrophilic attack, indicating electron acceptance, while green or black single-barbed "fishhook" arrows denote the movement of single electrons in radical processes.

Aromatic carbons C4, C5, C6 dominate nucleophilic reactivity (f^- = 0.193–0.192), identifying them as primary – OH attack sites. Elevated f^+ (0.117–0.099) signals ambiphilic character – susceptible to both electrophilic and nucleophilic assault. High f^0 (0.155–0.146) indicates significant radical-pathway contribution. This distribution – concentrated on the aromatic ring—reflects aqueous polarization shifting reactivity from halogen-centered (nonpolar) to ring carbon sites (Table 5) (Ak and Kebiroglu, 2023; Jumabaev et al., 2025; Zamiran et al., 2025).

C13, C16 show inverted profiles: moderate f^+ (0.117, 0.103) with low f^- (0.035, 0.036), denoting electrophilic character and poor nucleophilic response. Minimal f^0 (0.076, 0.070) suggests radical resistance.

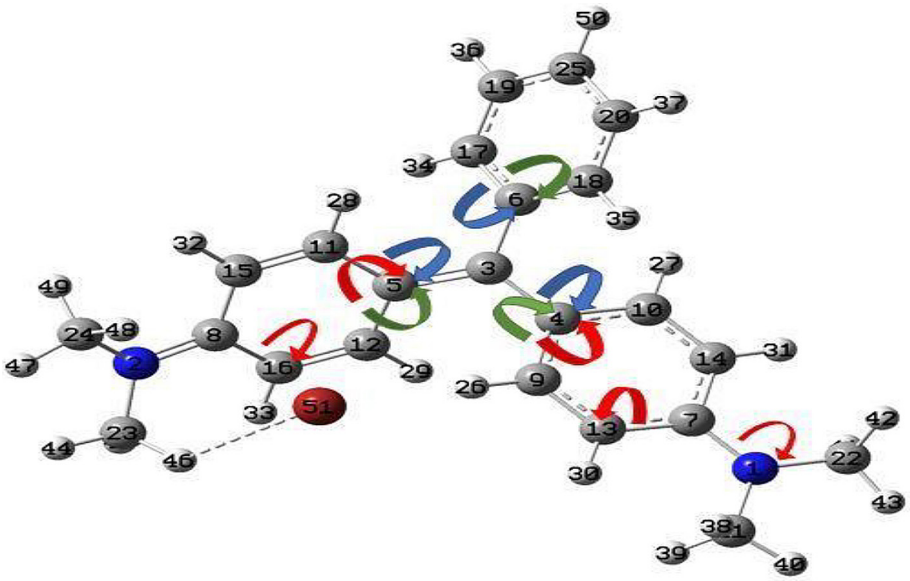

Figure 3. MG-Cl^- Fukui profile in water

N1 exhibits balanced reactivity (f^+ = 0.102, f^- = 0.043, f^0 = 0.073), secondary to aromatic carbons but non-negligible—particularly for radical pathways via lone-pair delocalization.

MG-Cl^- undergoes multi-site degradation: initial - OH attack on nucleophilic C4–C6 (f^- ≈ 0.19) initiates ring-opening; secondary electrophilic assault on C13–C16 and radical involvement at aromatic sites yield fragmentation and eventual mineralization (Ak and Kebiroglu, 2023; Jumabaev et al., 2025; Zamiran et al., 2025).

MG-Br^- exhibits comparable aromatic nucleophilicity (C5 f^- = 0.1941, matching MG-Cl; C4 f^- = 0.1408, slightly lower). C5 distinguishes itself as the dominant reactive site across all indices (f^+ = 0.107, f^- = 0.194, f^0 = 0.150), indicating preferential degradation initiation. C13 shows heightened f^+ (0.1293, +9% vs. MG-Cl), suggesting enhanced electrophilicity consistent with bromine's polarizability enabling radical recombination (Table 6) (Ak and Kebiroglu, 2023; Zamiran et al., 2025). N1 reactivity mirrors MG-Cl but remains moderate (f^- = 0.040, lower than Cl counterpart), limiting nitrogen-centered degradation pathways.

MG-Br-'s C13 elevation signals competitive radical mechanisms absent in MG-Cl, explaining Br's alternative degradation flexibility (Table 7). (Ak and Kebiroglu, 2023; Kim et al., 2013; Zamiran et al., 2025).

Table 5. Key atoms Fukui Indices for MG-Cl^-

Atom	f^+	f^-	f^0
C4	0.1175	0.1933	0.1554
C5	0.1084	0.1899	0.1492
C6	0.0991	0.1929	0.1460
C13	0.1175	0.0351	0.0763
C16	0.1031	0.0362	0.0696
N1	0.1024	0.0426	0.0725

Table 6. Key atoms Fukui Indices for MG-Br^-

Atom	f^+	f^-	f^0
C4	0.0840	0.1408	0.1124
C5	0.1069	0.1941	0.1505
C6	0.0718	0.1572	0.1145
C13	0.1293	0.0510	0.0902
N1	0.1026	0.0401	0.0714

Chlorine and bromine counterions distinctly modulate MG reactivity profiles. MG-Cl^+ concentrates nucleophilic reactivity at aromatic sites (f^- = 0.19, C4–C6), favoring rapid - OH-initiated ring scission through ionic pathways observed experimentally. Conversely, MG-Br^+ balances nucleophilic aromatic sites (C5, f^- = 0.19) and electrophilic C13 (f^+ = 0.129), enabling hybrid radical/

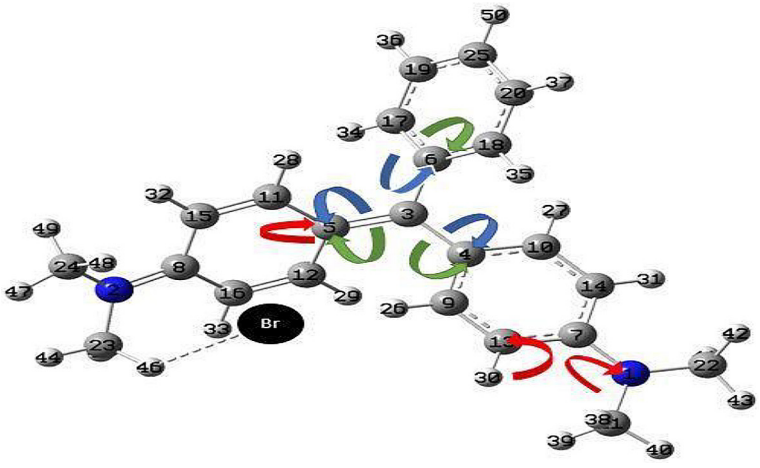

Figure 4. MG-Br^- Fukui profile in water

Table 7. Comparative halogen analysis of Fukui indices results

Metric	MG-Cl-	MG-Br-	Interpretation
C4–C6 avg f^-	0.191	0.157	Cl > Br nucleophilicity (–18%)
C5 f^0 (radical)	0.149	0.150	Equivalent radical susceptibility
C13 f^+	0.118	0.129	Br > Cl electrophilicity (+9%)

nucleophilic mechanisms that dominate at elevated pH. Fukui mapping identifies C5 as the universal reactive hotspot for both derivatives, with site-specific f^-/f^+ distributions explaining pH selectivity: acidic conditions promote SET/nucleophilic attack, while basic conditions favor C13 radical coupling (Ak and Kebiroglu, 2023; Jumabaev et al., 2025; Zamiran et al., 2025). These results provide molecular guidance for designing advanced oxidation processes targeting aromatic degradation in recalcitrant dyes (Adole, 2023; Ak and Kebiroglu, 2023).(Adole, 2023; Ak and Kebiroglu, 2023; Jumabaev et al., 2025; Zamiran et al., 2025).

CONCLUSIONS

This comprehensive density functional theory investigation (M06-2X/6-31++G (d,p)) elucidates quantum-chemical mechanisms governing oxidative degradation of malachite green (Basic Green 4, MG^+) and commercial halide formulations ($MG\text{-}Cl^-$, $MG\text{-}Br^-$) in aqueous media. Halogenation transforms the electronic landscape—reducing HOMO-LUMO gap by ~15% (4.79 → 4.17–4.18 eV), amplifying electrophilicity 3.7-fold (ω = 5.29 eV), and enhancing polarity (μ = 28.16 D) – overcoming MG^+ intrinsic kinetic recalcitrance.

Multiscale analysis reveals halide-specific control beyond solubility: Cl^- achieves thermodynamic optimality (ΔG = –1.94 kJ/mol) via maximal entropic stabilization and optimal hydration surfaces (A^+ = 291 Å²), promoting rapid SET/nucleophilic ring scission at aromatic hotspots (C4–C6, $f^- \approx 0.19$); Br^- enables hybrid radical/nucleophilic pathways through C13 electrophilicity (f^+ = 0.129), yielding pH-dependent selectivity.

These findings establish the first quantitative structure-reactivity relationships linking halide identity, Fukui site-specific reactivity, solvation entropy, charge redistribution, and degradation kinetics for commercial MG dye. This molecular framework fills a critical knowledge gap and guides predictive design of halide-optimized advanced oxidation processes for recalcitrant cationic dyes.

Acknowledgements

The authors sincerely acknowledge the General Direction of Scientific Research and Technological Development of Algeria (DGRSDT) and the Ministry of Higher Education and Scientific Research of Algeria (MESRS) for their financial support.

REFERENCES

1. Abozeed, A. A., Younis, O., Al-Hossainy, A. F., El-Mawla, N. A., Sayed, M., A, M. K. E.-D., Tolba, M. S. (2022). Combined experimental and TD-DFT/DMOl(3) investigations, optical properties, and photoluminescence behavior of a thiazolopyrimidine derivative. *Sci Rep*, *12*(1), 15674. https://doi.org/10.1038/s41598-022-19840-y
2. Adole, V. A. (2023). DFT calculations on three 2,3-dihydrobenzofuran linked chalcones: Structural, HOMO-LUMO and spectroscopic (UV-Vis and IR) interpretation. *Vietnam Journal of Chemistry*, *61*(2), 147–157. https://doi.org/10.1002/vjch.202100023
3. Ait Tayeb, M. A., Tchouar, N., Miannay, F. A., Idrissi, A. (2021). Effect of the mixture composition of C4mimBF4/acetonitrile on the charge transfer in Coumarin 153: DFT and TD-DFT analysis. *Journal of Molecular Liquids*, *339*, 116830. https://doi.org/10.1016/j.molliq.2021.116830
4. Ak, F., Kebiroglu, H. (2023). Molecular structure, geometry properties, HOMO-LUMO, and MEP analysis of acrylic acid based on DFT calculations. *Journal of Physical Chemistry and Functional Materials*, *6*(2), 92–100. https://doi.org/10.54565/jphcfum.1343235
5. Ak, F., Kebiroglu, M. H. (2024). Spectroscopic characterizations and DFT Calculations of Olanzapine: Thermochemistry, HOMO-LUMO, FT-IR, MEP, and Hirshfeld Surface (HS) Analyses [Olanzapinin Spektroskopik Karakterizasyonları ve DFT Hesaplamaları: Termokimya, HOMO-LUMO, FT-IR, MEP ve Hirshfeld Yüzey (HS) Analizleri]. *Yüzüncü Yıl Üniversitesi Fen Bilimleri Enstitüsü Dergisi*, *29*(3), 854–867. https://doi.org/10.53433/yyufbed.1413089
6. Anwer, H., Mahmood, A., Lee, J., Kim, K.-H., Park, J.-W., Yip, A. C. K. (2019). Photocatalysts for degradation of dyes in industrial effluents: Opportunities and challenges. *Nano Research*, *12*(5), 955–972. https://doi.org/10.1007/s12274-019-2287-0
7. Aziz, A., Khan, E., Kabir, A., Soomro, R., Nawaz, S., Riaz, A.,…Muhammad, S. (2025). Advanced oxidation processes for the abatement of emerging contaminants in wastewater: A critical review of mechanisms, applications, and future trajectories. *Indus Journal of Bioscience Research*, *3*(11), 143-152. https://doi.org/10.70749/ijbr.v3i11.2656
8. Barone, V., Cossi, M. (1998). Quantum calculation of molecular energies and energy gradients in solution by a conductor solvent model. *The Journal of Physical Chemistry A*, *102*(11), 1995–2001. https://doi.org/10.1021/jp9716997
9. Becke, A. D. (1992). Density-functional thermochemistry. I. The effect of the exchange-only gradient correction. *The Journal of Chemical Physics*, *96*(3),

2155–2160. https://doi.org/10.1063/1.462066 %J

10. Bendaas, R., Bekkar, Y., Messaadia, L., Bourougaa, L., Messaoudi, A., Kiamouche, S., Messaoud, B. (2024). Computational-based investigation of antioxidative potential polyphenolic compounds of Salvia officinalis L.: combined DFT and molecular docking approaches. *J Mol Model*, *30*(3), 87. https://doi.org/10.1007/s00894-024-05866-8
11. Bills, T. D., Marking, L. L., Chandler, J. H. J. I. i. F. C. (1977). Malachite green: its toxicity to aquatic organisms, persistence, and removal with activated carbon. 0–6.
12. Bock, S., Al-Owaedi, O. A., Eaves, S. G., Milan, D. C., Lemmer, M., Skelton, B. W.,…Low, P. J. (2017). Single-molecule conductance studies of organometallic complexes bearing 3-thienyl contacting groups. *Chemistry*, *23*(9), 2133–2143. https://doi.org/10.1002/chem.201604565
13. Chai, J.-D., Head-Gordon, M. (2008). Long-range corrected hybrid density functionals with damped atom–atom dispersion corrections [10.1039/B810189B]. *Physical Chemistry Chemical Physics*, *10*(44), 6615–6620. https://doi.org/10.1039/B810189B
14. Ersanlı, C. C., Yoğurtçu, H. N. (2025). Structural parameters, NLO, HOMO, LUMO, MEP, chemical reactivity descriptors, Mulliken-NPA, thermodynamic functions, hirshfeld surface analysis and molecular docking of 1,3-Bis(4-methylphenyl) triazine [Structural Parameters, NLO, HOMO, LUMO, MEP, chemical reactivity descriptors, Mulliken-NPA, thermodynamic functions, hirshfeld surface analysis and molecular docking of 1,3-Bis(4-methylphenyl)triazine]. *International Scientific and Vocational Studies Journal*, *9*(1), 130–144. https://doi.org/10.47897/bilmes.1697802
15. Fatimah, I., Fadillah, G., Yanti, I., Doong, R.-a. (2022). Clay-supported metal oxide nanoparticles in catalytic advanced oxidation processes: A review. *Nanomaterials*, *12*(5), 825.
16. Frisch, M., Trucks, G., Schlegel, H., Scuseria, G., Robb, M., Cheeseman, J.,…Petersson, G. J. G. I. W. C. (2009). Gaussian 09 Revision D. *The Royal Society of Chemistry 1*, 51.
17. Gao, Y., Zhu, W., Li, J., Liu, W., Li, X., Zhang, J., Huang, T. (2022). Anthraquinone acted as a catalyst for the removal of triphenylmethane dye containing tertiary amino group: Characteristics and mechanism. *Journal of Environmental Sciences*, *121*, 148–158. https://doi.org/10.1016/j.jes.2021.09.024
18. Ghime, D., Goru, P., Ojha, S., Ghosh, P. (2019). Oxidative decolorization of a malachite green oxalate dye through the photochemical advanced oxidation processes [Journal article]. *Global Nest Journal*, *21*(2), 195–203.
19. He, J., Mo, P., Luo, Y.-S., Yang, P.-H. (2023). Strategies for solving the issue of malachite green residues in aquatic products: A review. *Aquaculture Research*, *2023*(1), 8578570. https://doi.org/10.1155/2023/8578570
20. Jumabaev, A., Khudaykulov, B., Holikulov, U., Norkulov, A., Subbiah, J., Al-Dossary, O. M.,…Issaoui, N. (2025). Molecular structure, vibrational spectral assignments, MEP, HOMO-LUMO, AIM, NCI, RDG, ELF, LOL properties of acetophenone and for its solutions based on DFT calculations. *Optical Materials*, *159*, 116683. https://doi.org/10.1016/j.optmat.2025.116683
21. Kenouche, S., Sandoval-Yañez, C., Martínez-Araya, J. I. (2022). The antioxidant capacity of myricetin. A molecular electrostatic potential analysis based on DFT calculations. *Chemical Physics Letters*, *801*, 139708. https://doi.org/10.1016/j.cplett.2022.139708
22. Khaled, N. A., Ibrahim, M. A., Mohamed, N. A., Ahmed, S. A., Ahmed, N. S. (2024). DFT studies on N-(1-(2-bromobenzoyl)-4-cyano-1H-pyrazol-5-yl). *Spectrochim Acta A Mol Biomol Spectrosc*, *323*, 124864. https://doi.org/10.1016/j.saa.2024.124864
23. Khalid, M., Hussain, R., Hussain, A., Ali, B., Jaleel, F., Imran, M.,…Jahrukh Tariq, C. (2019). Electron donor and acceptor influence on the nonlinear optical response of diacetylene-functionalized organic materials (DFOMs): Density functional theory calculations. *Molecules*, *24*(11), 2096.
24. Kim, B.-G., Ma, X., Chen, C., Ie, Y., Coir, E. W., Hashemi, H.,…Kim, J. (2013). Energy level modulation of HOMO, LUMO, and band-gap in conjugated polymers for organic photovoltaic applications. *Advanced Functional Materials*, *23*(4), 439–445. https://doi.org/10.1002/adfm.201201385
25. Li, G., Peng, L., Ding, Z., Liu, Y., Gu, Z., Zhang, L., Shi, G. (2014). Decolorization and biodegradation of triphenylmethane dyes by a novel *Rhodococcus qingshengii* JB301 isolated from sawdust. *Annals of Microbiology*, *64*(4), 1575–1586. https://doi.org/10.1007/s13213-014-0801-7
26. Lu, T. (2024). A comprehensive electron wavefunction analysis toolbox for chemists, Multiwfn. *The Journal of Chemical Physics*, *161*(8). https://doi.org/10.1063/5.0216272
27. Lu, T., Chen, F. (2012). Multiwfn: A multifunctional wavefunction analyzer. *Journal of Computational Chemistry*, *33*(5), 580–592. https://doi.org/10.1002/jcc.22885
28. Moumen, A., Belhocine, Y., Sbei, N., Rahali, S., Ali, F. A. M., Mechati, F.,…Seydou, M. (2022). Removal of malachite green dye from aqueous solution by catalytic wet oxidation technique using Ni/Kaolin as catalyst. *Molecules*, *27*(21). https://doi.org/10.3390/molecules27217528
29. Mulliken, R. S. (1955). Electronic population

analysis on LCAO–MO molecular wave functions. I. *The Journal of Chemical Physics*, *23*(10), 1833–1840. https://doi.org/10.1063/1.1740588

30. Murray, J. S., Politzer, P. (2011). The electrostatic potential: an overview. *WIREs Computational Molecular Science*, *1*(2), 153–163. https://doi.org/10.1002/wcms.19
31. Nascimento, M. A., LaPierre, E. A., Patrick, B. O., Watson, J. E. T., Watanabe, L., Rawson, J.,… Manners, I. (2024). 1,3-Dipolar cyclisation reactions of nitriles with sterically encumbered cyclic triphosphanes: synthesis and electronic structure of phosphorus-rich heterocycles with tunable colour [10.1039/D4SC02497D]. *Chemical Science*, *15*(30), 12006012016. https://doi.org/10.1039/D4SC02497D
32. Parr, R. G., Pearson, R. G. (1983). Absolute hardness: companion parameter to absolute electronegativity. *Journal of the American Chemical Society*, *105*(26), 7512–7516. https://doi.org/10.1021/ja00364a005
33. Prabhu, C., Rajesh, P., Lawrence, M., Sahaya Jude Dhas, S., Almansour, A. I. (2025). Computational aspects of DFT, HOMO-LUMO, PED, molecular docking and basic characterisations of Octadec-9-Enoic Acid (C18H34O2). *Molecular Physics*, *123*(4), e2385572. https://doi.org/10.1080/00268976.2024.2385572
34. Rather, R. A., Mir, J. M., Bhat, M. A., Shalla, A. H. (2025). Design and DFT-based optimization of a GO-containing guar gum hydrogel for dye removal [10.1039/D5MA00389J]. *Materials Advances*, *6*(16), 5648–5666. https://doi.org/10.1039/D5MA00389J
35. Rayaroth, M. P., Boczkaj, G., Aubry, O., Aravind, U. K., Aravindakumar, C. T. (2023). Advanced oxidation processes for degradation of water pollutants—ambivalent impact of carbonate species: A review. *Water*, *15*(8), 1615.
36. Roohi, H., Facehi, A., Ghauri, K. (2020). Adsorption of cytarabine and gemcitabine anticancer drugs on the BNNT surface: DFT and GD3-DFT approaches. *Adsorption*, *26*(8), 1365–1384. https://doi.org/10.1007/s10450-020-00247-y
37. Sjoberg, P., Murray, J. S., Brinck, T., Politzer, P. (1990). Average local ionization energies on the molecular surfaces of aromatic systems as guides to chemical reactivity. *Canadian Journal of Chemistry*, *68*(8), 1440–1443. https://doi.org/10.1139/v90-220
38. Slicker, K., Delgado, A., Jiang, J., Tang, W., Cronin, A., Blackwell, R. E.,…Fischer, F. R. (2024). Engineering small HOMO-LUMO gaps in polycyclic aromatic hydrocarbons with topologically protected states. *Nano Lett*, *24*(17), 5387–5392. https://doi.org/10.1021/acs.nanolett.4c01476
39. Song, Y., Guan, S., Wang, Y., Zhang, C., Liu, J., Zhang, L. (2025). The application of hydrodynamic cavitation technology and the synergistic effect of hybrid advanced oxidation processes: a review. *Water Science and Technology*, *92*(2), 301–325. https://doi.org/10.2166/wst.2025.102
40. Sundari, S. S., Mehala, M., Arunadevi, N., Kanchana, P., Alharthi, S. S., Kumar, E. R.,…El-Rehim, A. F. A. (2023). Structural and optical properties of salicyl-N-methyl-4-stilbazolium tosylate: Thermal, DFT, MEP and Hirshfeld surface analysis. *Journal of Molecular Structure*, *1271*, 134072. https://doi.org/10.1016/j.molstruc.2022.134072
41. Toghiani, J., Malekzadeh, S., Jamali, N., Afsham, N., Fallah, N., Mahboubi, A.,…Oladzad, S. (2024). Novel advanced oxidation processes (AOPs) as lignocellulosic biomass pretreatment approaches and their sustainability assessment: A review. *Current Pollution Reports*, *10*(2), 207–46. https://doi.org/10.1007/s40726-024-00295-w
42. Yang, W., Mortier, W. J. (1986). The use of global and local molecular parameters for the analysis of the gas-phase basicity of amines. *Journal of the American Chemical Society*, *108*(19), 5708–5711. https://doi.org/10.1021/ja00279a008
43. Yaseen, M., Khan, A., Khan, K., Shah, M. (2025). Degradation of malachite green (MG) under Uv and Uv with H_2O_2 processes. *Annual Methodological Archive Research Review*, *3*, 22–35. https://doi.org/10.63075/7a0cbe22
44. Zamiran, F., Mohammadi Ziarani, G., Feizi-Dehnayebi, M., Mirhosseyni, M., Badiei, A., Abu-Dief, Ahmed M. (2025). Design, preparation, characterization, density functional theory, and HOMO-LUMO perspective of Fe3O4@SiO2-Pr-NH-IC as a new nanomagnetic chemosensor. *Applied Organometallic Chemistry*, *39*(2), e7998. https://doi.org/https://doi.org/10.1002/aoc.7998
45. Zhao, Y., Truhlar, D. G. (2008). The M06 suite of density functionals for main group thermochemistry, thermochemical kinetics, noncovalent interactions, excited states, and transition elements: two new functionals and systematic testing of four M06-class functionals and 12 other functionals. *Theoretical Chemistry Accounts*, *120*(1), 215–241. https://doi.org/10.1007/s00214-007-0310-x
46. Zhou, X.-J., Guo, W.-Q., Yang, S.-S., Zheng, H.-S., Ren, N.-Q. (2013). Ultrasonic-assisted ozone oxidation process of triphenylmethane dye degradation: Evidence for the promotion effects of ultrasonic on malachite green decolorization and degradation mechanism. *Bioresource Technology*, *128*, 827–830. https://doi.org/10.1016/j.biortech.2012.10.086